photonics

MDPI

Article

Quantitative Evaluation of the Phase Function Effects on Light Scattering and Radiative Transfer in Dispersed Systems

Lanxin Ma [1,2], Lechuan Hu [1,2], Chengwei Jia [1,2], Chengchao Wang [1,2] and Linhua Liu [1,2,*]

[1] School of Energy and Power Engineering, Shandong University, Jinan 250061, China
[2] Optics & Thermal Radiation Research Center, Institute of Frontier and Interdisciplinary Science, Shandong University, Qingdao 266237, China
* Correspondence: liulinhua@sdu.edu.cn

Abstract: The light scattering properties of particles play important roles in radiative transfer in many dispersed systems, such as turbid atmosphere, ocean water, nanofluids, composite coatings and so on. As one of the scattering property parameters, the scattering phase functions of particles are strongly dependent on the particle size, size distribution, and morphology, as well as on the complex refractive indices of the particles and surrounding media. For the sake of simplicity, the empirical phase function models are widely used in many practical applications. In this work, we focus on the radiative transfer problem in dispersed systems composed of spherical particles, and give quantitative analyses of the impact of scattering phase functions on the radiative transfer process. We fit the scattering phase functions of four different types of practical dispersed systems using four previously proposed empirical phase function models, including the Henyey–Greenstein (HG) model, Cornette Shanks (CS) model, Reynold and McCormick (RM) model and two-term Reynolds–McCormick (TTRM) model. By comparing the radiative transfer characteristics (i.e., hemispherical reflectance, hemispherical transmittance and total absorptance) of dispersed layers calculated using the Monte Carlo method, the relative errors caused by using the empirical phase functions are systematically investigated. The results demonstrate that the HG, CS and RM models cause obvious errors in the calculation of hemispherical reflectance in many cases. Meanwhile, the induced errors show no obvious regularity, but are related to the particle size and layer optical thickness. Due to the good fitting effect in both forward and backward directions, the TTRM model provides significantly higher performances in fitting the phase functions of all considered cases than the widely used single-term parametrizations. Moreover, for different particle sizes and layer optical thicknesses, the induced errors of the TTRM model in radiative transfer characteristics are very small, especially for the case of polydisperse particles. Our results can be used to guide the design, analysis and optimization of dispersed systems in practical optics and photonics applications.

Keywords: scattering phase function; light scattering; radiative transfer; Mie scattering; Monte Carlo simulation

Citation: Ma, L.; Hu, L.; Jia, C.; Wang, C.; Liu, L. Quantitative Evaluation of the Phase Function Effects on Light Scattering and Radiative Transfer in Dispersed Systems. *Photonics* **2022**, *9*, 584. https://doi.org/10.3390/photonics9080584

Received: 25 July 2022
Accepted: 17 August 2022
Published: 18 August 2022

1. Introduction

Light scattering and radiative transfer in dispersed systems are of great importance in many fields of natural sciences and engineering, such as remote sensing and modelling of the ocean and atmosphere, biomedical imaging and diagnostics, photocatalytic and photothermal techniques and so on [1–5]. In the theoretical analysis and experimental study of radiative transfer processes in such dispersed systems, the fundamental optical/radiative properties of particles, such as the absorption coefficient μ_{abs}, scattering coefficient μ_{sca}, extinction coefficient μ_{ext} and scattering phase function $\Phi(\theta)$ (or volume scattering function $\beta(\theta)$, VSF) should be obtained first [6,7]. Those optical properties of particles are determined by the chemical composition, size, shape, volume fraction and mixing state, and are generally obtained through the electromagnetic scattering calculation or experimental measurement [8,9].

With the development of optical measurement technology, the measurement of light attenuation and absorption is advanced for both laboratory and field measuring, whereas the scattering phase functions or VSF are rare and difficult to measured, due to the complicated measurement geometries and the difficulty of achieving accurate measurements at forward and backward scattering angles [2,10]. Specifically, the range of scattering energy over all scattering angles typically reaches 5 or 6 orders of magnitude in many cases, which necessitates high measurement accuracy in photodetectors. As a consequence, the mechanical design of the instruments for scattering phase function measurements is often very complicated, and only several prototype sensors with broad angular ranges exist [11,12]. Lee and Lewis [13] developed a prototype VSF sensor (MVSM) for the measurement of the VSF of the ocean, which resolves the VSF from 0.6° to 177.3° in 0.3° increments at eight wavelengths. Twardowski et al. [14] introduced a prototype VSF sensor (MASCOT), which measures the VSF at angles spanning 10° to 170° in 10° increments. Babin et al. [15] described a methodology for determining the VSF of aqueous particle suspensions from measurements with a laboratory multi-angle light scattering instrument called DAWN. Tan et al. [16] presented a novel optical approach to measure the volume scattering function (VSF) by image detection, which realizes the scattering angle measurement from 8° to 172° at 1° intervals. Wu et al. [17] developed a laboratory-based VSF instrument adopting the periscopic optical system, which can realize the measurement of VSF in the range of 1–178.5°. Moreover, Sequoia Scientific Inc developed a commercial instrument (LISST–VSF) for measuring the VSF in situ or in the laboratory for angles 0.1–150° at a 515 nm wavelength [18]. Overall, although related experimental techniques and studies regarding the measurement of scattering phase functions or VSFs have been extensively conducted in the past decade, the spectral distributions of the scattering phase function for most particles remain mostly unknown because of the lack of direct measurement.

If we know the distributions of size, shape, internal structure and the complex refractive index for particles, the optical properties of particles can be accurately calculated. The common calculation methods include Lorentz–Mie theory [8], discrete dipole approximation (DDA) [19], T-matrix method [20], geometric optical approximation [21] and so on. However, it should be noted that it is usually difficult to obtain all these geometric and physical parameters of dispersed media. Therefore, many empirical phase function models have been developed and used in numerical simulations of radiative transfer in dispersed systems, such as the Henyey–Greenstein (HG) model [22], Cornette Shanks (CS) model [23], Fournier–Forand (FF) model [24], Reynold and McCormick (RM) model [25], and two-term Reynolds–McCormick (TTRM) model [26]. Mobley et al. [27] conducted numerical simulations of the phase function effects on oceanic light fields. The results show that the shape of the phase function can have a significant effect on the underwater radiances, irradiances and reflectances. Bodenschatz et al. [28] carried out a quantitative analysis of the influences of different scattering phase functions on subdiffusive backscattered light. Moreover, the authors introduced a new parameter that more accurately relates a scattering phase function to its subdiffusive backscattering intensity. Vaudelle [29] proposed an approximate analytical effective phase function from a thin slab, which can realize the fast estimation of the asymmetry factor of turbid media. Miramirkhani et al. [30] assessed the effect of scattering phase functions on underwater visible light communication channel models and demonstrated that the simplified phase function models (one-term or two-term HG models) result in a large discrepancy of channel gain in a typical underwater scenario. Wang et al. [26] proposed a five-parameter two-term Reynolds–McCormick (TTRM) phase function model and compared it with eight different empirical models. The results indicated that the TTRM model provides the best fit to the experimental results in all cases. Moreover, according to the measurements of sediments and microalgae, Harmel et al. [31] demonstrated that the TTRM model provides significantly higher performances in fitting the phase functions of actual living or mineral hydrosols than the widely used single-term phase function models.

Although many studies on the scattering phase function models and their related applications have been carried out, due to the complexity of the scattering phase function, there is still no universal phase function model that can comprehensively represent the scattering properties of different kinds of particles. In addition, the influences of the empirical phase function models on the radiative transfer process are still lacking in systematic evaluation. In this work, the radiative transfer characteristics of four different types of dispersed media (SiO_2, TiO_2, Si and Au spherical particles embedded in water) are investigated to quantitatively assess the influence of the empirical phase function models (HG, CS, RM and TTRM) on radiative transfer. The single-scattering properties of spherical particles are calculated using Lorenz–Mie theory. HG and CS phase functions are calculated by using the asymmetry factor. RM and TTRM phase functions are obtained by fitting the Mie phase function. The directional–hemispherical reflectance, directional–hemispherical transmittance and the total absorptance for a plane-parallel layer of spherical particles are calculated and compared using the Monte Carlo method. In order to further characterize the effects of scattering phase functions on radiative transfer, the errors of the radiative transfer characteristics calculated using four empirical phase function models relative to the Mie-calculated phase function are compared. The influences of particle sizes, size distributions and layer optical thicknesses are discussed. The goal of this work is to elucidate how and to what extent the empirical phase function models influence the radiative transfer characteristic of dispersed media.

2. Model and Methods

2.1. Radiative Transfer Model

We considered radiative energy transfer in a plane-parallel layer composed of sparsely dispersed spherical particles, as shown in Figure 1. The spherical particles with radius r and complex refractive index $m_p = n_p + i\kappa_p$ were randomly dispersed in a non-absorbing host medium with refractive index n_{host}. To avoid the influences of Fresnel reflections from the boundaries, the refractive index of the host medium was set to equal that of the surrounding medium. For simplicity, the incident wavelength λ was set to 0.6 μm. In each case, the conventional gamma distribution of particle radii defined by Hansen and Travis [32] was used:

$$n(r) = \text{constant} \times r^{(1-3b)/b} \exp\left(-\frac{r}{ab}\right), b \in (0, 0.5) \quad (1)$$

where the constant was chosen such that the size distribution satisfied the standard normalization $\int_0^\infty n(r)dr = 1$. Two important characteristics of the size distribution were the effective radius r_{eff} and effective variance v_{eff} defined by:

$$r_{eff} = \frac{1}{\langle G \rangle_r} \int_{r_{min}}^{r_{max}} \pi r^3 n(r) dr \quad (2)$$

$$v_{eff} = \frac{1}{\langle G \rangle_r r_{eff}^2} \int_{r_{min}}^{r_{max}} (r - r_{eff})^2 \pi r^2 n(r) dr \quad (3)$$

where $\langle G \rangle_r = \int_{r_{min}}^{r_{max}} \pi r^2 n(r) dr$ was the average area of the geometric projection per particle, and r_{max} and r_{min} represented the maximum and minimum radius of the particles. Note that for the gamma distribution with $r_{min} = 0$ and $r_{min} = \infty$, a and b coincided with r_{eff} and v_{eff}, and the distribution with $v_{eff} = 0$ corresponded to monodisperse particles.

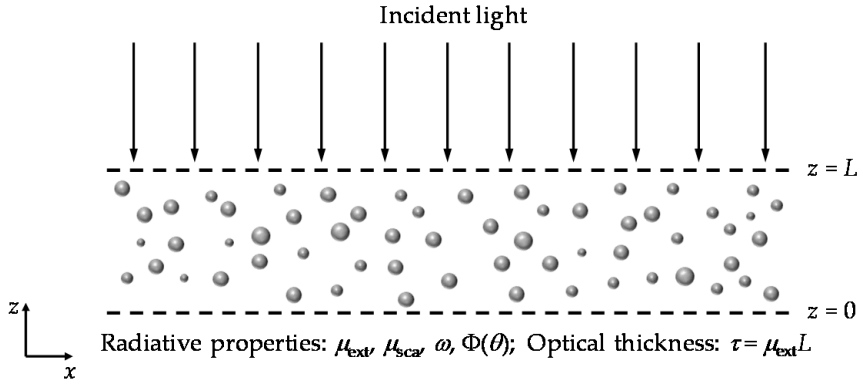

Figure 1. Schematic of the plane-parallel layer composed of sparse dispersed spherical particles.

It must be emphasized that the radiative transfer model presented in this paper is based on the independent scattering approximation, which means the dependent scattering effect or near-field coupling effect were not considered [33–35]. Under the framework of independent scattering theory, the radiative/optical properties of the dispersed systems, including the extinction coefficient μ_{ext}, scattering coefficient μ_{sca} and scattering phase function $\Phi(\theta)$, can be calculated as [6,9]:

$$\mu_{\text{sca}} = \mu_{\text{sca,p}} = n_0 \int_{r_{\min}}^{r_{\max}} n(r) C_{\text{sca}}(r) dr = \frac{f_{\text{v}}}{\langle V \rangle_r} \langle C_{\text{sca}} \rangle_r \tag{4}$$

$$\mu_{\text{ext}} = \mu_{\text{ext,p}} = n_0 \int_{r_{\min}}^{r_{\max}} n(r) C_{\text{ext}}(r) dr = \frac{f_{\text{v}}}{\langle V \rangle_r} \langle C_{\text{ext}} \rangle_r \tag{5}$$

$$\Phi(\theta) = \frac{n_0}{\mu_{\text{sca}}} \int_{r_{\min}}^{r_{\max}} C_{\text{sca}}(r) \Phi_{\text{p}}(r, \theta) n(r) dr \tag{6}$$

where $\mu_{\text{ext,p}}$ and $\mu_{\text{sca,p}}$ are the extinction coefficient and scattering coefficient of the particles, $\langle C_{\text{ext}} \rangle_r$ and $\langle C_{\text{sca}} \rangle_r$ are the ensemble-averaged extinction cross section and scattering cross section per particle, C_{ext}, C_{sca} and Φ_{p} are the far-field extinction cross section, scattering cross section and scattering phase function of single particles, respectively, and can be calculated using the Lorenz–Mie theory [8,36]. n_0 is the number of particles per unit volume of discrete random medium, $\langle V \rangle_r = 4\pi \int_{r_{\min}}^{r_{\max}} r^3 n(r) dr/3$ is the average volume per particle, and $f_{\text{v}} = 4\pi n_0 \int_{r_{\min}}^{r_{\max}} r^3 n(r) dr/3$ is the volume fraction of the particles.

2.2. Empirical Phase Functions

Four previously proposed empirical phase function models, including the HG model, CS model, RM model, and TTRM model, are studied and discussed herein. The HG model is one of the most widely used empirical phase functions, and is a function of the asymmetry factor with the following analytic form [22]:

$$\Phi_{\text{HG}}(\theta, g) = \frac{1}{4\pi} \frac{1 - g^2}{[1 + g^2 - 2g\cos\theta]^{3/2}} \tag{7}$$

where g is the asymmetry factor and related to the phase function by:

$$g = \frac{1}{4\pi} \int_{4\pi} \Phi(\theta) \cos\theta d\Omega \tag{8}$$

The value of g ranges from backscattering (-1) through isotropic scattering (0) to forward scattering (1).

Similarly to the HG phase function, the CS phase function is a function of the asymmetry factor g, and has the following form [23]:

$$\Phi_{CS}(\theta, g) = \frac{3\left[1+\cos^2\theta\right]}{2(2+g^2)} \frac{1-g^2}{\left[1+g^2-2g\cos\theta\right]^{3/2}} \tag{9}$$

The CS phase function is mainly suitable for characterizing the scattering by small particles. It converges to the Rayleigh phase function when $g = 0$, and it approaches the HG phase function when $g = 1$.

The RM phase function, which was proposed by Reynold and McCormick [25], describes highly anisotropic angular scattering distributions and has the following form:

$$\Phi_{RM}(\theta, \overline{g}, \alpha) = \frac{\alpha\overline{g}\left(1-\overline{g}^2\right)^{2\alpha}}{\pi\left[1+\overline{g}^2-2\overline{g}\cos\theta\right]^{\alpha+1}\left[(1+\overline{g})^{2\alpha}-(1-\overline{g})^{2\alpha}\right]} \tag{10}$$

where $\overline{g}$ and α are two fitting parameters. Note that the RM phase function approaches the HG phase function when $\alpha = 0.5$, and only in this situation does the parameter $\overline{g}$ have the same meaning of asymmetry factor g. The two-term TTRM phase function, which was recently proposed by Wang et al. [26], is a modification of the RM phase function, introducing a mixing parameter γ, as follows:

$$\Phi_{TTRM}(\theta, g_1, \alpha_1, g_2, \alpha_2, \gamma) = \gamma\Phi_{RM}(\theta, g_1, \alpha_1) + (1-\gamma)\Phi_{RM}(\theta, g_2, \alpha_2) \tag{11}$$

This function has two parts with two different parameters, where g_1 is positive and g_2 is negative, in order to treat the forward and backward peaks in the phase function. The parameter γ gives the forward scattering portion while $(1-\gamma)$ is the backward scattering portion. Meanwhile, in order to assess the fitting effects of the RM and TTRM phase functions, a loss function, which is defined as the mean square logarithmic error (MSLE) between the fitting results Φ_{Model} and Mie results Φ_{Mie} is used [31]:

$$MSLE = \frac{\sum_{\theta_i=0}^{\theta_i=\pi}\left[\log\Phi_{Mie}(\theta_i) - \log\Phi_{Model}(\theta_i)\right]^2}{N_{sca} - N_{param}} \tag{12}$$

where N_{sca} is the number of scattering angles of the phase function and N_{param} is the number of fitting parameters of the phase function model ($N_{param} = 2$ for RM model and $N_{param} = 5$ for TTRM model). By using a large number of fitting parameters, the RM and TTRM phase functions can be well-fitted with the Mie phase function. In this work, the fitting procedure is based on the particle swarm optimization algorithm under given bound constraint values (see supporting material, Table S1).

2.3. Radiative Transfer Calculation

Multiple scatterings of light in the dispersed systems are accounted for by the meanings of the radiative transfer equation (RTE), which can be written as [6,7]:

$$\frac{dI(\tau)}{d\tau} = -I(\tau) + \frac{\omega}{4\pi}\int_{4\pi} I\left(\tau, \vec{\Omega'}\right)\Phi\left(\vec{\Omega'}, \vec{\Omega}\right)\mathrm{d}\,\Omega' \tag{13}$$

where I is the radiation intensity in the direction of $\vec{\Omega}$, $\tau = \mu_{ext}L$ is the optical thickness of the dispersed layer, L is the geometric thickness of the dispersed layer, $\omega = \mu_{sca}/\mu_{ext}$ is the single scattering albedo, and Ω' is the solid angle. We note that the thermal radiation term was neglected in this study, and the RTE was solved by using the widely used Monte Carlo (MC) method [6,37]. A light beam was perpendicularly incident on the boundary ($z = 0$) of the layer by default. After interacting with the layer, the reflected and transmitted photons

were collected, and the directional–hemispherical reflectance R, directional–hemispherical transmittance T and the total absorbance A of the dispersed layer were finally determined:

$$R = \frac{N_r}{N_0} \tag{14}$$

$$T = \frac{N_t}{N_0} \tag{15}$$

$$A = 1 - R - T \tag{16}$$

where N_0 is the total number of the photons that are incident on the layer, and N_r and N_t are the number of photons that are collected with the use of detectors positioned in the hemispherical space outside the upper surface and the lower surface, respectively. In this study, 5×10^6 photons were used for each calculation to obtain accurate results without using too much computation time.

3. Results and Discussion

To theoretically investigate the influence of the scattering phase function on a practical radiative transfer process, the radiative transfer characteristics of four different types of dispersed systems were studied in this paper. Firstly, Lorenz–Mie theory considering the particle size distribution was used to calculate the far-field extinction cross section, scattering cross section, scattering phase function, and the asymmetry factor of the particles. Secondly, HG and CS phase functions were calculated by using the asymmetry factor g. Additionally, RM and TTRM phase functions were obtained by fitting the Mie phase function. Lastly, radiative transfer characteristics (i.e., R, T and A) of the dispersed media were calculated and compared using the MC method on account of the Mie phase function, HG, CS, RM and TTRM phase functions.

In order to cover more comprehensive and more realistic situations, four different types of dispersed systems with a wide range of particle sizes ($x_{\text{eff}} = 2\pi n_{\text{host}} r_{\text{eff}} / \lambda = 1.0$, 2.0, 5.0 and 10.0, respectively) and size distributions ($v_{\text{eff}} = 0$, 0.01, 0.05 and 0.15, respectively) were studied in this paper. For simplicity, the incident wavelength λ was set to 0.6 μm; the complex refractive indices of spherical particles m_{p} and water host medium n_{host} for the four cases are listed in Table 1. Note that these four cases can be considered as the situation of micro–nano particles embedded in water, which is common in many practical applications, such as photothermal, photocatalytic and optical visualization [38–41]. In Case 1 and Case 2, both the particles and media were non-absorbing. In Case 3 and Case 4, absorbing particles with higher and lower refractive indices were embedded in the non-absorbing water medium. The radiative properties of different monodisperse and polydisperse size distributions of spheres are given in the supporting material, Table S2.

Table 1. Four different types of spherical particles embedded in water (λ = 0.6 μm).

Number	Materials of Particles	m_{p} (Particles)	n_{host} (Water) [42]
Case 1	Silicon dioxide (SiO_2)	1.458 + 0i [43]	1.333
Case 2	Titanium dioxide (TiO_2)	2.605 + 0i [44]	1.333
Case 3	Silicon (Si)	3.949 + 0.0274i [45]	1.333
Case 4	Gold (Au)	0.249 + 3.074i [46]	1.333

3.1. Scattering Phase Functions of Monodisperse and Polydisperse Spherical Particles

The Mie phase functions considering the size distribution of particles, as characterized by conventional gamma distributions with effective particle size parameter x_{eff} equal to 1.0, 2.0, 5.0 and 10.0 and effective variance v_{eff} equal to 0, 0.01, 0.05 and 0.15 were calculated. Meanwhile, HG and CS phase functions were calculated on account of the asymmetry factor g, and the RM and TTRM empirical phase functions were fitted to the calculated Mie phase functions. The specific parameters obtained by fitting the Mie scattering phase func-

tion with RM and TTRM models are shown in the supporting material, Tables S3 and S4. All MSLE numbers for the TTRM model were less than 0.1, and most of them were less than 0.01, demonstrating the validity of our parameter fitting [31]. Parameters γ, g_1 and g_2 varied greatly from case to case. Since the upper and lower limits of parameters α_1 and α_2 were set at -5 to 5, the cases that reached the upper and lower limits needed further optimization with extended limits. In this work, we did not carry out further optimizations, considering the MSLEs to be acceptable. Moreover, it was observed that for most cases, the retrieved α parameters obviously departed from the 0.5 value considered in the HG model [31]. In general, if the exact phase functions are known (e.g., Mie phase functions), the TTRM model can fit well to the exact phase functions by choosing appropriate fitting parameters. However, if accurate calculations are not performed first, the data of phase functions should be obtained based on a significant number of measurements, and if possible in a high angular resolution manner [26,31].

Figure 2 presents the comparison of the Mie phase function with four phase function empirical models for SiO_2 particles embedded in water (Case 1). Overall, the scattering pattern became more anisotropic, and forward scattering became more dominant with increasing particle size. Meanwhile, we can observe that the HG and CS phase functions had poor overlaps with the Mie phase functions in most circumstances, especially for forward and backward scattering. The RM phase function showed good agreement with the Mie phase functions, apart from some situations involving small size particles with $x_{\text{eff}} = 1.0$. In most cases, the results showed that the TTRM functions fit better to the Mie phase functions than the HG, CS and RM phase functions, but some discrepancies appeared when there were oscillations in the Mie calculations, owing to excitations of higher order eigenmodes for large size particles in the monodisperse situations with $v_{\text{eff}} = 0$, as shown in Figure 2c,d. Nevertheless, TTRM function still followed the trend, although it did not describe the multiple peaks. Such scattering phase function oscillations were smoothed for polydisperse situations with increasing effective variance v_{eff} due to the averaging procedure. Considering that the particles were polydisperse in most practical applications, TTRM phase function could fit Mie calculations within a wide range of particle sizes and distributions. Moreover, the TTRM outperformed the other models even when scattering angles are larger than 140°. This result implies that the TTRM could provide a new means to extrapolate phase function measurements when instrumentation is limited in the backward directions [26].

We also present Mie calculations and phase function fittings for monodisperse ($v_{\text{eff}} = 0$) and polydisperse ($v_{\text{eff}} = 0.05$) TiO_2 particles (Case 2, with refractive index $n_{\text{p}} = 2.605$), as shown in Figure 3. The fitting effects of the HG phase function for $x_{\text{eff}} = 2$ were better than the CS and RM phase functions. Compared with Case 1 (SiO_2 particles with $n_{\text{p}} = 1.458$), the higher refractive index of particles led to stronger backward scattering, especially for larger size particles. Meanwhile, it was found that the difference between forward scattering and backward scattering became smaller. Multiple peaks also appeared when x_{eff} was larger than 1.0, and the oscillations in the phase function were obviously reduced for polydisperse situations. The RM phase function showed poor overlap with the Mie phase functions for backward scattering due to its simple expression. By introducing a mixing parameter, the TTRM was able to sufficiently characterize the forward and backward peaks in the phase function. As shown in Figure 3d,h, for large size particles with $x_{\text{eff}} = 10$, the TTRM model outperformed the other models over the full range of scattering angles, although the forward and backward scattering peaks were very high.

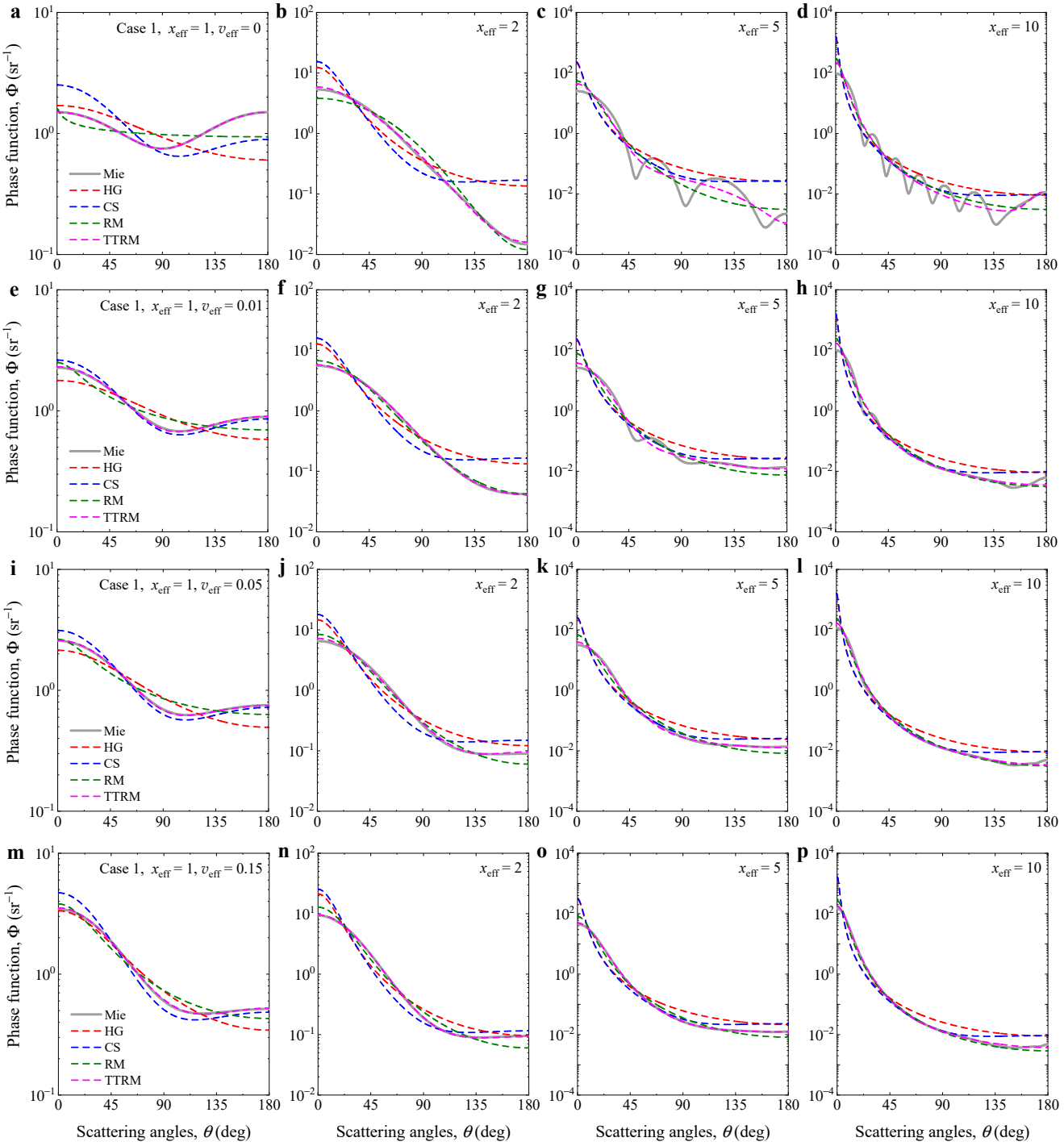

Figure 2. Comparison of the Mie phase function with four phase function empirical models for SiO_2 particles (Case 1) with (**a**–**d**) v_{eff} = 0, (**e**–**h**) v_{eff} = 0.01, (**i**–**l**) v_{eff} = 0.05, and (**m**–**p**) v_{eff} = 0.15, respectively.

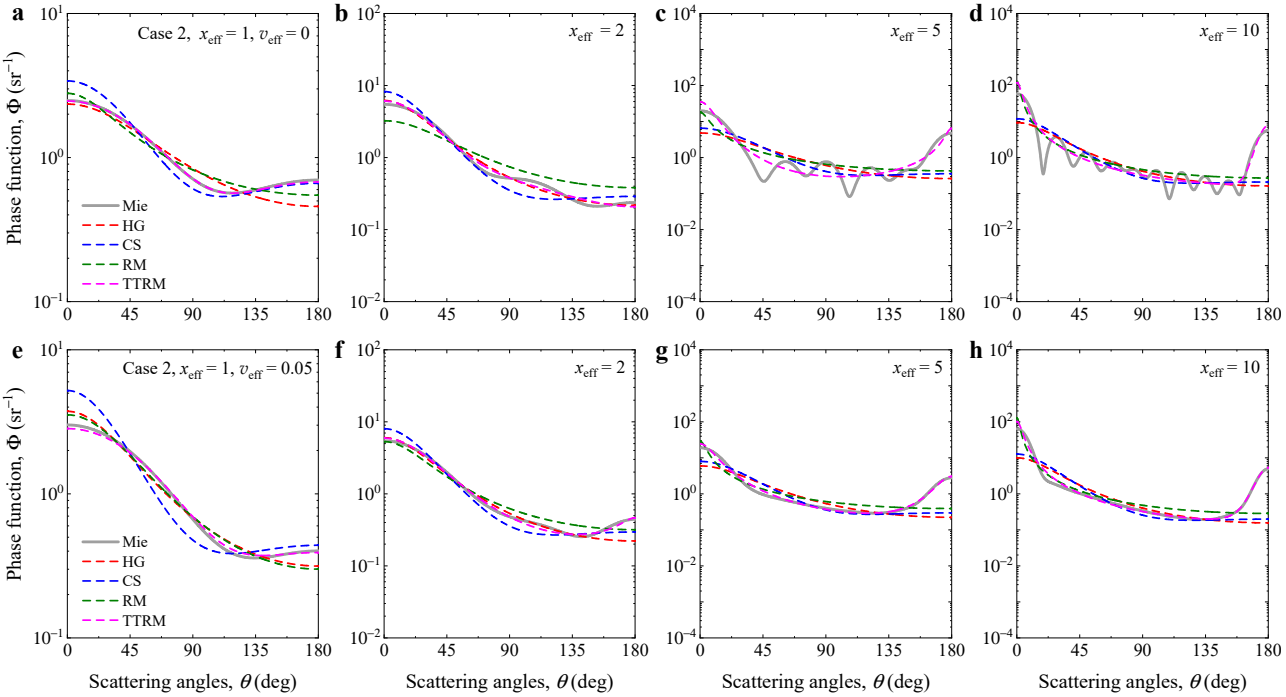

Figure 3. Comparison of the Mie phase function with four phase function empirical models for TiO_2 particles (Case 2) with (**a**–**d**) v_{eff} = 0 and (**e**–**h**) v_{eff} = 0.05, respectively.

To study the effect of particle absorption on scattering phase functions, we performed Mie calculations and phase function fittings for Si particles and Au particles embedded in water, as shown in Figures 4 and 5. In general, the forward scattering increased markedly with increasing particle size parameter. However, a peculiar phenomenon occurred: the forward scattering was even weaker than the backward scattering for monodisperse Si particles with x_{eff} = 2.0, as shown in Figure 4b. This result is mainly attributed to the Mie resonances of high refractive-index dielectric particles [41,47]. In some cases, the antiphase interference of the electric dipole and magnetic dipole modes resulted in the radiation pattern of particles dominated by backward scattering. When the effective variance v_{eff} increased to 0.05, due to the averaging procedure, the phenomenon of the forward scattering being greater than the backscattering disappeared, as indicated in Figure 4f. By comparing the Mie phase functions with the phase functions obtained from the four empirical phase function models, it was also found that the TTRM model outperformed the other models over the full range of scattering angles for both the cases of Si particles and Au particles. However, for the other three empirical models, the fitting effects were unstable and depended on circumstances. For example, the RM model fit the Mie phase function well in the forward directions, but poorly in the backward directions, as shown in Figure 4a,e. In general, because of the simple form of the three empirical models (HG, CS and RM), it was difficult for these models to remain consistent with the Mie phase function in all scattering angles. In addition, it should be noted that the four empirical phase function models could be used for both spherical and non-spherical particles if the exact phase functions, measured data or necessary parameters (e.g., asymmetry factors need to be given for HG and CS models) were known. The phase function effects on light scattering and radiative transfer in dispersed systems composed of non-spherical particles will be investigated in future work.

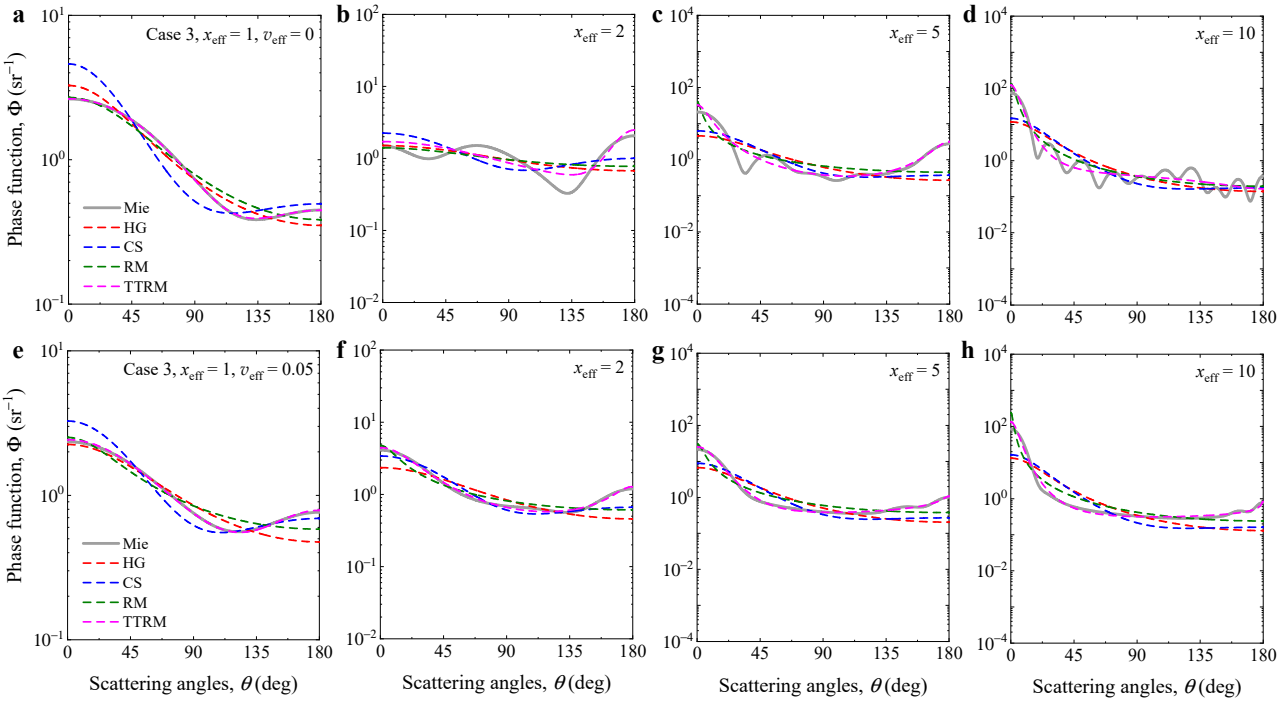

Figure 4. Comparison of the Mie phase function with four phase function empirical models for Si particles (Case 3) with (**a**–**d**) v_{eff} = 0 and (**e**–**h**) v_{eff} = 0.05, respectively.

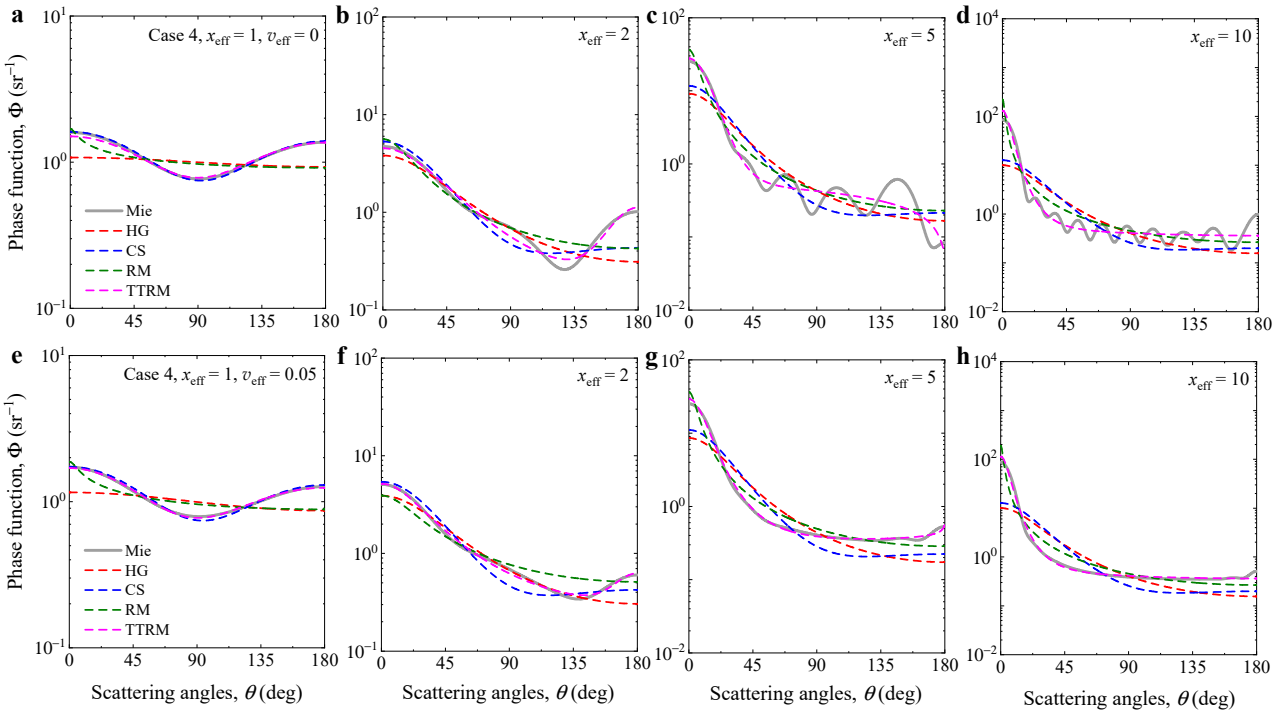

Figure 5. Comparison of the Mie phase function with four phase function empirical models for Au particles (Case 4) with (**a**–**d**) v_{eff} = 0 and (**e**–**h**) v_{eff} = 0.05, respectively.

3.2. Radiative Transfer Characteristics of the Dispersed Layer

The radiative transfer process can be affected by many factors. The most direct way to describe the effects of multiple scattering between particles on radiative transfer is to solve the RTE to obtain the apparent reflection, transmission and absorption characteristics of the dispersed systems. In this section, the directional-hemispherical reflectance *R*, directional-

hemispherical transmittance T and total absorptance A of the dispersed layer are calculated using the MC method on account of the Mie, HG, CS, RM and TTRM phase functions. To further characterize the effects of scattering phase functions on the radiative transfer process, the errors of the radiative transfer characteristics (R, T and A) caused by using the empirical phase function models are obtained and analyzed. The relative errors are defined according to $\delta_\xi = |\xi_{\mathrm{Mie}} - \xi_{\mathrm{EM}}|/\xi_{\mathrm{Mie}} \times 100\%$, where ξ_{Mie} and ξ_{EM} refer to the characteristic parameters (R, T and A) obtained by using the Mie phase function and empirical phase function models, respectively.

3.2.1. Case 1: Non-Absorbing SiO_2 Particles Embedded in Water

Figures 6 and 7 present the hemispherical reflectances R of the dispersed plane-parallel layer (for Case 1 with non-absorbing SiO_2 particles embedded in water) as functions of the layer optical thickness for monodisperse ($v_{\mathrm{eff}} = 0$) and polydisperse ($v_{\mathrm{eff}} = 0.05$) particles, respectively. Insets are logarithmic plots of the corresponding reflectance. The figures also include the relative errors δ_R of the hemispherical reflectances caused by using the empirical phase function models. As shown in the figures, the hemispherical reflectance is relatively small for media with a small optical thickness (e.g., $\tau < 1.0$), and such reflectance calculated using HG phase function is extremely inaccurate. The corresponding relative errors may be more than 100% for some circumstances when $x_{\mathrm{eff}} = 5.0$ and 10.0. Accordingly, small reflectance corresponds to high transmittance (Figures S1 and S2 in the supplement material) and the relative errors of hemispherical transmittance will be small. As the spectral reflectance of ocean seawater is mostly within 0.05 [37,48], the relative errors of the reflectance calculated using HG and CS phase functions are extremely large under this background. With increasing optical thickness, the reflectance of the dispersed layer increases, along with reducing relative errors in different degrees for the reflectance calculated by the four different phase functions. Besides the layer optical thickness, the size parameter x_{eff} of particles also has a significant influence on the relative error δ_R. The smaller the size parameter is, the closer the particle scattering is to Rayleigh scattering, and the less influence the scattering phase function shows on the reflection characteristics. With increasing particle size parameters, the particle scattering effect enhances, especially the forward scattering, which leads to the decrease in the hemispherical reflectance of the dispersed layer and the increase in the influence of scattering phase function on the radiative transfer process.

According to the foregoing results, the fitting effect of RM phase function is contingent for some situations; thus, the relative error of the hemispherical reflectance calculated by RM phase function is also contingent, especially for the case of monodisperse particles. As shown in Figure 6f,g, for dispersed layers with $x_{\mathrm{eff}} = 2.0$ and 5.0, the maximum relative errors of reflectance can reach up to about 40% and 50%, respectively. However, when $x_{\mathrm{eff}} = 1.0$ and 10.0, the maximum relative errors of reflectance decrease to about 7% and 26%, respectively. By comparison, the relative errors of the hemispherical reflectance calculated by the TTRM models are very small for different particle sizes and layer optical thicknesses, especially for the case of polydisperse particles. This is because the TTRM empirical phase function models have good fitting effects in both forward and backward directions, as indicated in Figure 2. Meanwhile, it should be noted that for monodisperse particle systems, the relative errors of the hemispherical reflectance induced by using the TTRM models are still uncertain because the TTRM model cannot perfectly fit all the characteristics of Mie phase function.

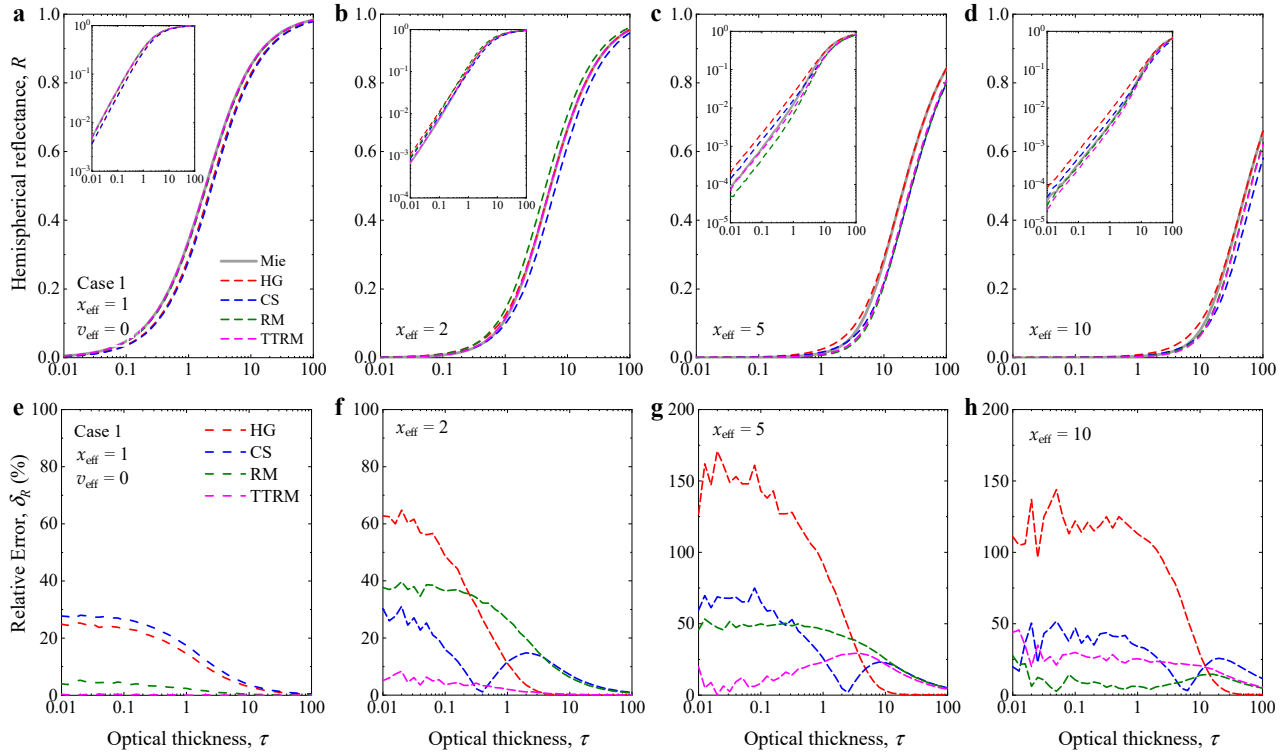

Figure 6. The hemispherical reflectance of the layers (Case 1, SiO_2 particles, v_{eff} = 0) versus the layer optical thickness for different phase function models, and the relative errors of the hemispherical reflectance caused by using four phase function empirical models. (**a**–**h**) The insets show a Log–Log plot of the reflectance versus optical thickness.

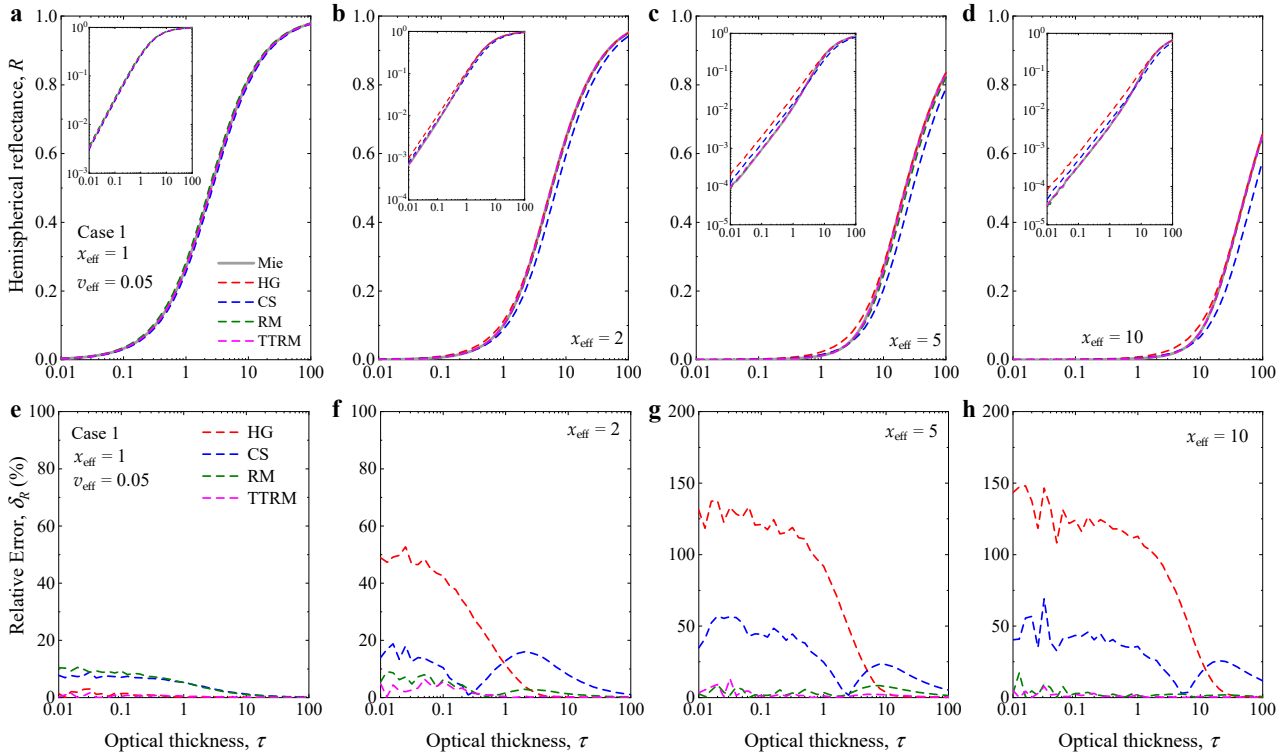

Figure 7. As in Figure 6, but for effective variance v_{eff} = 0.05. (**a**–**h**) The insets show a Log–Log plot of the reflectance versus optical thickness.

3.2.2. Case 2: Non-Absorbing TiO_2 Particles Embedded in Water

Figures 8 and 9 present the hemispherical reflectances R of the dispersed plane-parallel layer (for Case 2 with non-absorbing TiO_2 particles embedded in water) and the relative errors δ_R of the hemispherical reflectance caused by using four phase function empirical models as functions of the layer optical thickness for monodisperse ($v_{\text{eff}} = 0$) and polydisperse ($v_{\text{eff}} = 0.05$) particles, respectively. As shown in the figures, the relative errors of hemispherical reflectance calculated using HG phase function for particle size parameter $x_{\text{eff}} = 1.0$ and 2.0 are less than 10%. At this point, the performance of the HG phase function model in radiative transfer process is better than that of CS and RM models. It is worth noting that the overlap between the HG and Mie phase functions is not good, especially for forward and backward scattering, as Figure 3 shows, demonstrating that the general fitting effect may also result in a higher coincidence of radiative transfer characteristics. According to the forgoing results, the fitting effect of the RM phase function is contingent on some situations; thus, the relative error of the hemispherical reflectance calculated by RM phase function is also contingent, for example, on the relative error of RM-calculated hemispherical reflectance being larger than CS and HG phase functions for $x = 2$ situations.

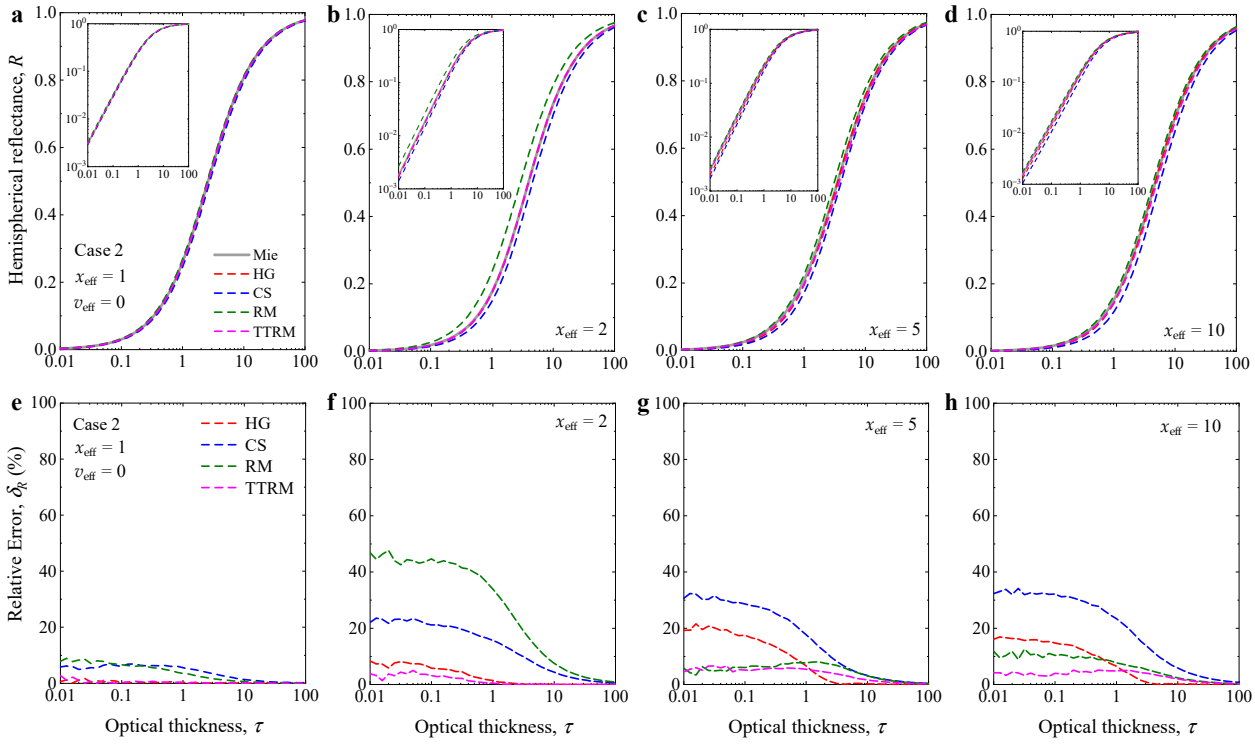

Figure 8. The hemispherical reflectance of the layers (Case 2, TiO_2 particles, $v_{\text{eff}} = 0$) versus the layer optical thickness for different phase function models, and the relative errors of the hemispherical reflectance caused by using four phase function empirical models. (**a**–**h**) The insets show a Log–Log plot of the reflectance versus optical thickness.

Compared with Case 1 (SiO_2 particles with $n = 1.458$), a higher refractive index of particles leads to stronger scattering and higher reflectance for large particle size situations. In general, the HG, CS and RM models will cause obvious errors in the calculation of hemispherical reflectance for unabsorbed particles in many cases. Although the induced error is related to the particle size and layer optical thickness, it is difficult to predict the specific error, and the errors show no obvious regularity. Meanwhile, it is gratifying to note that the TTRM empirical phase function model has high accuracy and strong adaptability in the calculation of hemispherical reflectances. For the cases of different particle size and layer thickness, the relative errors of hemispherical reflectance are less than 8%, which indicates that the TTRM model has excellent performance in radiative transfer calculations.

Moreover, as for the hemispherical transmittance (as shown in Figures S3 and S4), it was found that the relative errors induced by using the HG and TTRM models were very small, which indicates that the empirical phase function models can be used for radiative transfer calculations when focusing more on the transmission characteristics.

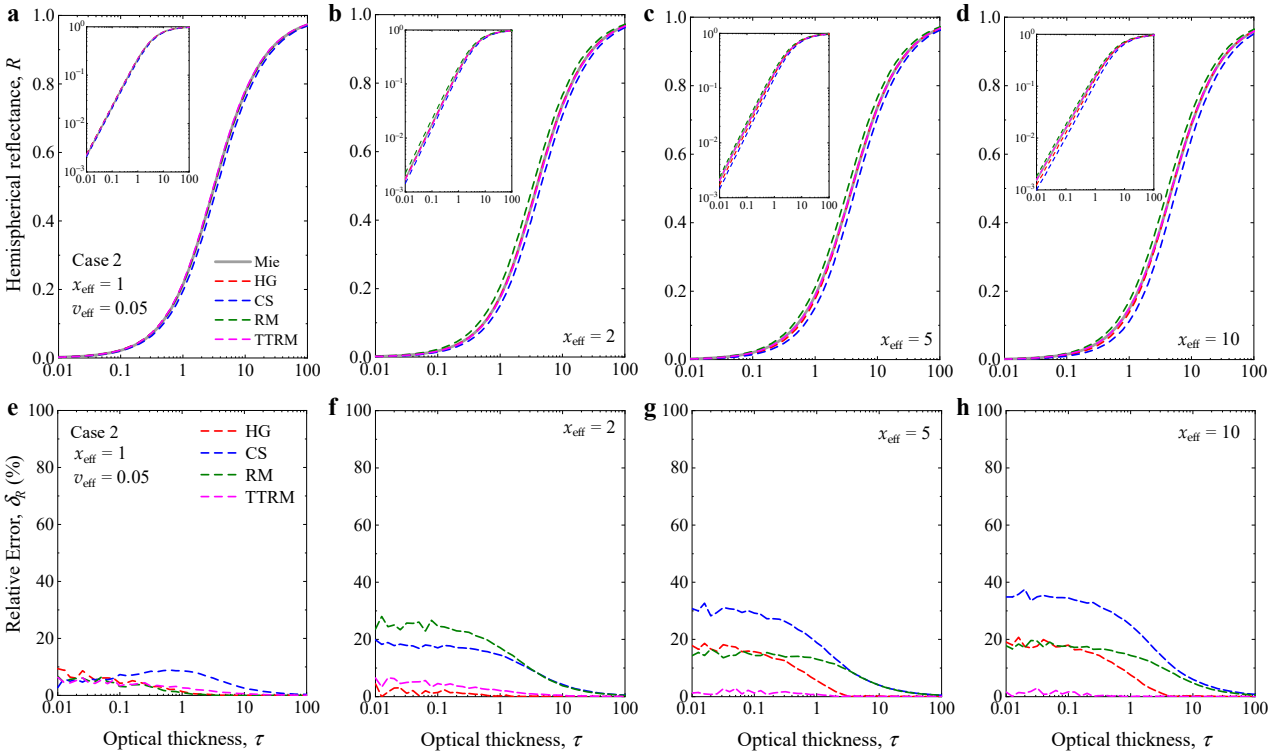

Figure 9. As in Figure 8, but for effective variance v_{eff} = 0.05. (**a**–**h**) The insets show a Log–Log plot of the reflectance versus optical thickness.

3.2.3. Case 3 and 4: Absorbing Si and Au Particles Embedded in Water

The hemispherical reflectance R of the layers (Case 3, absorbing Si particles with $v$eff = 0.05) versus the layer optical thickness for different phase function models and the relative errors δ_R of the hemispherical reflectance caused by using four phase function empirical models are presented in Figure 10. As shown, the hemispherical reflectances R of the layers tended to be constant with increasing optical thickness due to the strong absorption properties of Si particles. Moreover, unlike the results in Case 2 (as indicated in Figure 9), the relative errors δ_R caused by using the empirical phase function models showed no obvious decreasing trend with the increase in optical thickness. Furthermore, it was found that the reflectances calculated using HG and CS phase functions were generally smaller than those calculated on account of the Mie phase function. As the particle size parameter increased, due to the decrease in single scattering albedo (as shown in Table S2), the hemispherical reflectances R gradually decreased and the relative errors δ_R caused by using HG and CS phase functions showed an obvious increasing trend. As shown in Figure 10h, for large particles with x_{eff} = 10, the relative errors δ_R caused by using HG and CS phase functions were larger than 21.6% and 35% for all the considered optical thicknesses. Recent studies [41,47] show that Si nanoparticles have the lowest-order Mie resonance in the visible range and are widely used in the design of structural colors. Large reflectance errors will inevitably lead to large deviations in the optical and color characteristics. By comparison, the relative errors caused by using the RM and TTRM models are obviously smaller than those of HG and CS models. As presented in Figure 10e–h, the relative errors of TTRM-calculated hemispherical reflectance were within 10% for all the considered cases.

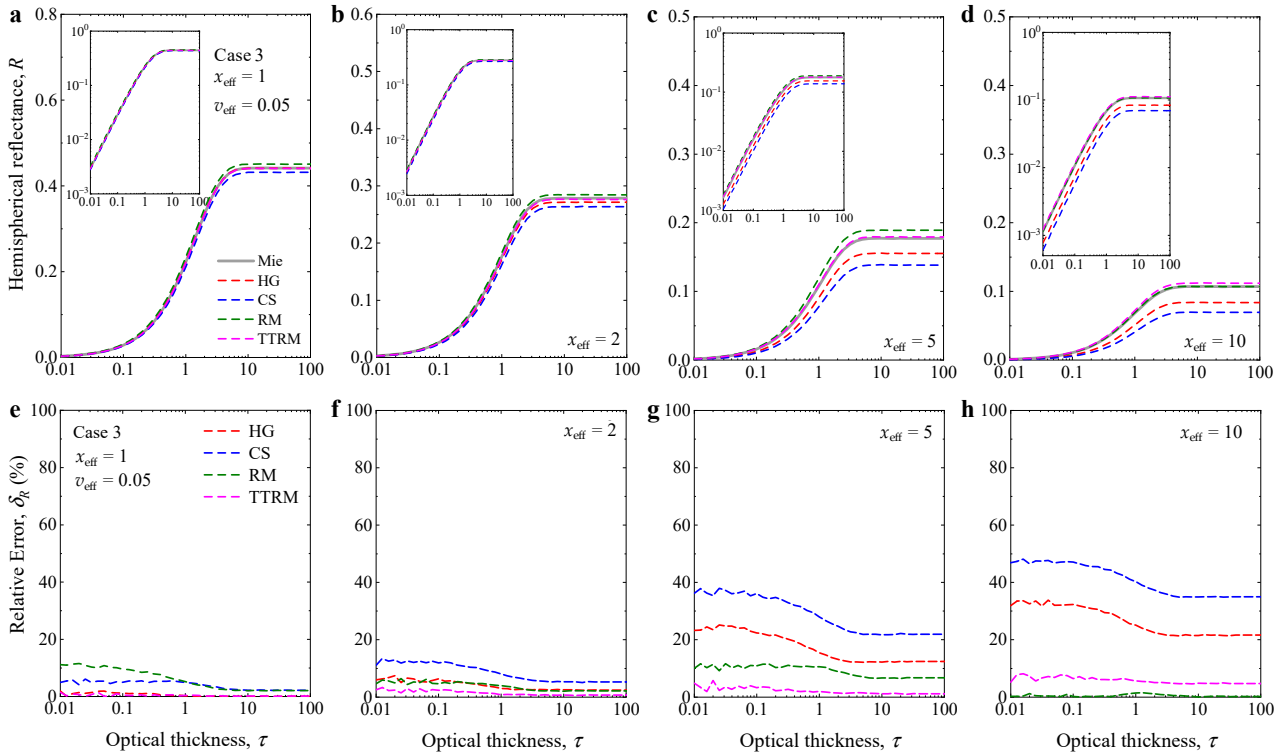

Figure 10. The hemispherical reflectance of the layers (Case 3, Si particles, v_{eff} = 0.05) versus the layer optical thickness for different phase function models, and the relative errors of the hemispherical reflectance caused by using four phase function empirical models. (**a**–**h**) The insets show a Log–Log plot of the reflectance versus optical thickness.

Considering the absorbance of the Si particles, we also present the total absorbance of the dispersed layers (Case 3, polydisperse particles with *v*eff = 0.05) and the corresponding relative errors caused by using four phase function empirical models in Figure 11. As shown, the total absorptance increased obviously with increasing particle size parameters due to the decrease in single scattering albedo. Meanwhile, similarly to the situation of hemispherical reflectance, the total absorptance showed a trend of increasing first and then gradually flattening out. In addition, although the relative errors caused by using different phase function models showed complex changes with the increase in optical thickness and particle size, all the relative errors were less than 6.4%. As for the TTRM model, the accuracy of the calculated absorptance was high, and the maximum relative error was only 0.6% for all the calculated results. Overall, all the four empirical scattering phase function models could be used for radiative transfer calculations when focusing more on the absorption characteristics of dispersed systems composed of absorbing Si particles.

We also present the hemispherical reflectance *R* and total absorbance *A* of the dispersed layers (Case 4, polydisperse Au particles with *v*eff = 0.05), and the corresponding relative errors caused by using four phase function empirical models in Figures S5 and S6. In general, the variation laws of relative errors in the reflectance and absorbance with particle size and layer optical thickness are basically similar to the corresponding situations of Si particles (Case 3). Owing to their strong interactions with visible light through localized surface plasmon resonances, Au nanoparticles have been subject to extensive research and application. According to the preceding analysis, the commonly used empirical phase function models (e.g., HG, CS, and RM) may cause obvious errors in the calculations of reflectance spectra and affect the accurate analysis of applications of plasmonic coloring and image projection [49,50]. Meanwhile, because the relative errors of absorption characteristics caused by using the empirical phase function models are relatively small, this

aspect can be ignored in many engineering applications, such as photothermal utilization and energy harvesting [51,52].

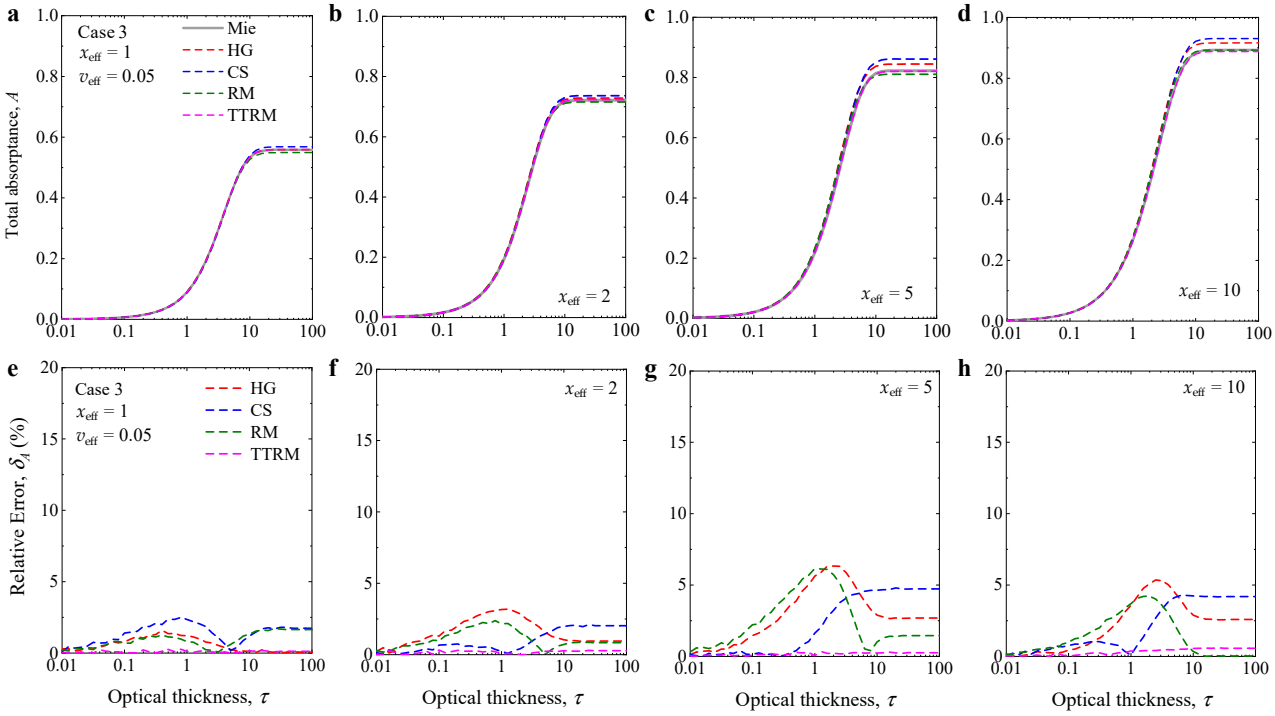

Figure 11. (**a**–**h**) The total absorptance of the layers (Case 3, Si particles, v_{eff} = 0.05) versus the layer optical thickness for different phase function models, and the relative errors of the absorptance caused by using four phase function empirical models.

4. Conclusions

In summary, we carried out systematic studies on the effects of scattering phase function on radiative transfer in realistic dispersed systems. By comparing with the Mie phase function, four empirical phase function models (HG, CS, RM and TTRM) were analyzed and discussed. To cover more comprehensive situations, the directional–hemispherical reflectance R, directional–hemispherical transmittance T and total absorptance A of four different types of dispersed systems with a wide range of particle sizes and size distributions were investigated using the Monte Carlo method.

The results demonstrate that the TTRM model provides significantly higher performances in fitting Mie phase functions than the widely used HG phase function and single-term RM models. Synthesizing the four application cases, it was found that the HG, CS and RM models caused obvious errors in the calculation of hemispherical reflectance in many cases. Meanwhile, the induced errors were related to the particle size and layer optical thickness, and it was difficult to predict the specific errors, with the errors showing no obvious regularity. The HG phase function is more suitable for the calculation conditions with smaller size parameters (x_{eff} = 1 and 2 in this study). CS phase function is not recommended because of its poor accuracy in most cases. The relative error of the hemispherical reflectance calculated by the RM phase function is contingent, especially for the case of monodisperse particles. Due to the good fitting effect in both forward and backward directions, the relative errors of the hemispherical reflectance calculated by the TTRM model are very small for different particle sizes and layer optical thicknesses, especially for the case of polydisperse particles. As for the dispersed systems composed of absorbing particles, because the relative errors of total absorptance are relatively small, all the four empirical scattering phase function models can be used for radiative transfer calculations when focusing more on the absorption characteristics in practical engineering applications. Our work gives quantitative analyses of the impacts of scattering phase function on the

light scattering and radiative transfer process, which can guide the design, analysis and optimization of dispersed systems in practical optics and photonics applications.

Supplementary Materials: The following supporting information can be downloaded at: https://www.mdpi.com/article/10.3390/photonics9080584/s1. Table S1: Values used as bound constraints in the fitting procedure for the RM and TTRM models; Table S2: Radiative properties of monodisperse and polydisperse particles for different particle size parameters; Table S3: Parameters obtained from fits to the RM function; Table S4: Parameters obtained from fits to the TTRM function; Figure S1: The hemispherical transmittance of the layers (Case 1, SiO_2 particles, v_{eff} = 0) versus the layer optical thickness for different phase function models, and the relative errors of the hemispherical transmittance caused by using four phase function empirical models; Figure S2: As in Figure S1, but for effective variance v_{eff} = 0.05; Figure S3: The hemispherical transmittance of the layers (Case 2, TiO_2 particles, v_{eff} = 0) versus the layer optical thickness for different phase function models, and the relative errors of the hemispherical transmittance caused by using four phase function empirical models; Figure S4: As in Figure S3, but for effective variance v_{eff} = 0.05; Figure S5: The hemispherical reflectance of the layers (Case 4, Au particles, v_{eff} = 0.05) versus the layer optical thickness for different phase function models, and the relative errors of the hemispherical transmittance caused by using four phase function empirical models; Figure S6: The total absorptance of the layers (Case 4, Au particles, v_{eff} = 0.05) versus the layer optical thickness for different phase function models, and the relative errors of the absorptance caused by using four phase function empirical models.

Author Contributions: Conceptualization, L.M. and L.L.; methodology, L.M., L.H. and C.J.; investigation, L.M., L.H. and C.J.; data curation, L.M., L.H. and C.W.; writing—original draft preparation, L.M. and C.W.; writing—review and editing, L.M. and C.W.; supervision, C.W. and L.L.; funding acquisition, L.M., C.W. and L.L. All authors have read and agreed to the published version of the manuscript.

Funding: National Natural Science Foundation of China (grant nos. 52076123, 51906127, 51806124), and China Postdoctoral Science Foundation (grant nos. 2019M662353, 2019M662354, 2021T140401, and 2020T130365).

Institutional Review Board Statement: Not applicable.

Informed Consent Statement: Not applicable.

Data Availability Statement: The data presented in this study are available on request from the corresponding author.

Acknowledgments: Lanxin Ma and Chengchao Wang gratefully acknowledge support from the Young Scholars Program of Shandong University.

Conflicts of Interest: The authors declare no conflict of interest.

References

1. Chowdhary, J.; Zhai, P.W.; Boss, E.S.; Dierssen, H.M.; Frouin, R.; Ibrahim, A.; Lee, Z.; Remer, L.A.; Twardowski, M.; Xu, F.; et al. Modeling atmosphere-ocean radiative transfer: A PACE mission perspective. *Front. Earth Sci.* **2019**, *7*, 100. [CrossRef]
2. Werdell, P.J.; McKinna, L.I.W.; Boss, E.S.; Ackleson, S.G.; Craig, S.E.; Gregg, W.W.; Lee, Z.; Maritorena, S.; Roesler, C.S.; Rousseaux, C.S.; et al. An overview of approaches and challenges for retrieving marine inherent optical properties from ocean color remote sensing. *Prog. Oceanogr.* **2018**, *160*, 186–212. [CrossRef] [PubMed]
3. Corrie, S.R.; Thurecht, K.J. Nano-bio interactions: Guiding the development of nanoparticle therapeutics, diagnostics, and imaging agents. *Pharm. Res.* **2016**, *33*, 2311–2313. [CrossRef] [PubMed]
4. Pivetta, T.P.; Botteon, C.E.A.; Ribeiro, P.A.; Marcato, P.D.; Raposo, M. Nanoparticle Systems for Cancer Phototherapy: An Overview. *Nanomaterials* **2021**, *11*, 3132. [CrossRef] [PubMed]
5. Bucharskaya, A.B.; Khlebtsov, N.G.; Khlebtsov, B.N.; Maslyakova, G.N.; Navolokin, N.A.; Genin, V.D.; Genina, E.A.; Tuchin, V.V. Photothermal and Photodynamic Therapy of Tumors with Plasmonic Nanoparticles: Challenges and Prospects. *Materials* **2022**, *15*, 1606. [CrossRef] [PubMed]
6. Modest, M.F. *Radiative Heat Transfer*; Academic Press: Cambridge, MA, USA, 2013.
7. Mishchenko, M.I.; Travis, L.D.; Lacis, A.A. *Multiple Scattering of Light by Particles*; Cambridge University Press: Cambridge, UK, 2006.
8. Bohren, C.F.; Huffman, D.R. *Absorption and Scattering of Light by Small Particles*; Wiely: New York, NY, USA, 1983.

9. Mishchenko, M.I.; Travis, L.D.; Lacis, A.A. *Scattering, Absorption, and Emission of Light by Small Particles*; Cambridge University Press: Cambridge, UK, 2002.
10. Pitarch, J.; Volpe, G.; Colella, S.; Santoleri, R.; Brando, V.E. Absorption correction and phase function shape effects on the closure of apparent optical properties. *Appl. Opt.* **2016**, *55*, 8618–8636. [CrossRef]
11. Harmel, T.; Hieronymi, M.; Slade, W.; Röttgers, R.; Roullier, F.; Chami, M. Laboratory experiments for inter-comparison of three volume scattering meters to measure angular scattering properties of hydrosols. *Opt. Express* **2016**, *24*, A234–A256. [CrossRef]
12. Chami, M.; Thirouard, A.; Harmel, T. POLVSM (Polarized Volume Scattering Meter) instrument: An innovative device to measure the directional and polarized scattering properties of hydrosols. *Opt. Express* **2014**, *22*, 26403–26428. [CrossRef] [PubMed]
13. Lee, M.E.-G.; Lewis, M. A New Method for the Measurement of the Optical Volume Scattering Function in the Upper Ocean. *J. Atmos. Ocean. Tech.* **2003**, *20*, 563–571. [CrossRef]
14. Twardowski, M.; Zhang, X.; Vagle, S.; Sullivan, J.M.; Freeman, S.A.; Czerski, H.; You, Y.; Bi, L.; Kattawar, G.W. The optical volume scattering function in a surf zone inverted to derive sediment and bubble particle subpopulations. *J. Geophys. Res. Oceans* **2012**, *117*, C00H17. [CrossRef]
15. Babin, M.; Stramski, D.; Reynolds, R.A.; Wright, V.M.; Leymarie, E. Determination of the volume scattering function of aqueous particle suspensions with a laboratory multi-angle light scattering instrument. *Appl. Opt.* **2012**, *51*, 3853–3873. [CrossRef] [PubMed]
16. Tan, H.; Doerffer, R.; Oishi, T.; Tanaka, A. A new approach to measure the volume scattering function. *Opt. Express* **2013**, *21*, 18697–18711. [CrossRef] [PubMed]
17. Wu, C.; Tao, B.; Guo, Y.; Huang, H.; Mao, Z.; Song, H.; Pan, D. Measurements of aquatic particle volume scattering function up to 178.5° in the east China sea. *Appl. Sci.* **2022**, *12*, 1894. [CrossRef]
18. Slade, W.H.; Agrawal, Y.C.; Mikkelsen, O.A. Comparison of measured and theoretical scattering and polarization properties of narrow size range irregular sediment particles. In Proceedings of the IEEE 2013 OCEANS-San Diego, San Diego, CA, USA, 23–27 September 2013; pp. 1–6.
19. Draine, B.T.; Flatau, P.J. Discrete-Dipole Approximation For Scattering Calculations. *J. Opt. Soc. Am. A* **1994**, *11*, 1491–1499. [CrossRef]
20. Mishchenko, M.I.; Travis, L.D.; Mackowski, D.W. T-matrix computations of light scattering by nonspherical particles: A review. *J. Quant. Spectr. Radiat. Trans.* **1996**, *55*, 535–575. [CrossRef]
21. Zhou, X.; Li, S.; Stamnes, K. Geometrical-optics code for computing the optical properties of large dielectric spheres. *Appl. Opt.* **2003**, *42*, 4295–4306. [CrossRef]
22. Henyey, L.C.; Greenstein, J.L. Diffuse radiation in the Galaxy. *Astrophys. J.* **1941**, *93*, 70–83. [CrossRef]
23. Cornette, W.M.; Shanks, J.G. Physically reasonable analytic expression for the single-scattering phase function. *Appl. Opt.* **1992**, *31*, 3152–3160. [CrossRef]
24. Fournier, G.; Forand, J.L. Analytic phase function for ocean water. *Ocean Opt. XII* **1994**, *2258*, 194–201.
25. Reynolds, L.O.; McCormick, N.J. Approximate two-parameter phase function for light scattering. *J. Opt. Soc. Am.* **1980**, *70*, 1206–1212. [CrossRef]
26. Wang, J.; Xu, C.; Nilsson, A.M.; Fernandes, D.L.A.; Niklasson, G.A. A novel phase function describing light scattering of layers containing colloidal nanospheres. *Nanoscale* **2019**, *11*, 7404–7413. [CrossRef]
27. Mobley, C.D.; Sundman, L.K.; Boss, E.S. Phase function effects on oceanic light fields. *Appl. Opt.* **2002**, *41*, 1035–1050. [CrossRef] [PubMed]
28. Bodenschatz, N.; Krauter, P.; Liemert, A.; Kienle, A. Quantifying phase function influence in subdiffusively backscattered light. *J. Biomed. Opt.* **2016**, *21*, 035002. [CrossRef] [PubMed]
29. Vaudelle, F. Approximate analytical effective phase function obtained for a thin slab geometry. *J. Quant. Spectr. Radiat. Trans.* **2017**, *193*, 47–56. [CrossRef]
30. Miramirkhani, F.; Karbalayghareh, M.; Uysal, M. Effect of scattering phase function on underwater visible light communication channel models. *Phys. Commun.* **2021**, *48*, 101410. [CrossRef]
31. Harmel, T.; Agagliate, J.; Hieronymi, M.; Gernez, P. Two-term Reynolds-McCormick phase function parameterization better describes light scattering by microalgae and mineral hydrosols. *Opt. Lett.* **2021**, *46*, 1860–1863. [CrossRef] [PubMed]
32. Hansen, J.E.; Travis, L.D. Light scattering in planetary atmospheres. *Space Sci. Rev.* **1974**, *16*, 527–610. [CrossRef]
33. Saulnier, P.M.; Zinkin, M.P.; Watson, G.H. Scatterer correlation effects on photon transport in dense random media. *Phys. Rev. B* **1990**, *42*, 2621–2623. [CrossRef]
34. Rezvani Naraghi, R.; Sukhov, S.V.; Sáenz, J.J.; Dogariu, A. Near-field effects in mesoscopic light transport. *Phys. Rev. Lett.* **2015**, *115*, 203903. [CrossRef]
35. Wu, R.; Dogariu, A. Nonstationary intensity statistics in diffusive waves. *Phys. Rev. Lett.* **2020**, *125*, 043902. [CrossRef]
36. Mishchenko, M.I.; Yang, P. Far-field Lorenz–Mie scattering in an absorbing host medium: Theoretical formalism and FORTRAN program. *J. Quant. Spectr. Radiat. Trans.* **2018**, *205*, 241–252. [CrossRef]
37. Ma, L.; Wang, F.; Wang, C.-A.; Wang, C.; Tan, J. Monte Carlo simulation of spectral reflectance and BRDF of the bubble layer in the upper ocean. *Opt. Express* **2015**, *23*, 24274–24289. [CrossRef] [PubMed]
38. Guan, X.; Du, J.; Meng, X.; Sun, Y.; Sun, B.; Hu, Q. Application of titanium dioxide in arsenic removal from water: A review. *J. Hazard. Mater.* **2012**, *215–216*, 1–16. [CrossRef] [PubMed]

39. Beicker, C.L.L.; Amjad, M.; Filho, E.P.B.; Wen, D. Experimental study of photothermal conversion using gold/water and MWCNT/water nanofluids. *Sol. Energy Mater. Sol. Cells* **2018**, *188*, 51–65. [CrossRef]
40. Abu-Hamdeh, N.H.; Alazwari, M.A.; Salilih, E.M.; Mohammad Sajadi, S.; Karimipour, A. Improve the efficiency and heat transfer rate' trend prediction of a flat-plate solar collector via a solar energy installation by examine the Titanium Dioxide/Silicon Dioxide-water nanofluid. *Sustain. Energy Technol. Assess.* **2021**, *48*, 101623. [CrossRef]
41. Sugimoto, H.; Okazaki, T.; Fujii, M. Mie Resonator Color Inks of Monodispersed and Perfectly Spherical Crystalline Silicon Nanoparticles. *Adv. Opt. Mater.* **2020**, *8*, 2000033. [CrossRef]
42. Segelstein, D.J. The Complex Refractive Index of Water. Ph.D. Thesis, University of Missour-Kansas City, Kansas City, MO, USA, 1981.
43. Malitson, I.H. Interspecimen Comparison of the Refractive Index of Fused Silica. *J. Opt. Soc. Am.* **1965**, *55*, 1205–1209. [CrossRef]
44. DeVore, J.R. Refractive Indices of Rutile and Sphalerite. *J. Opt. Soc. Am.* **1951**, *41*, 416–419. [CrossRef]
45. Aspnes, D.E.; Studna, A.A. Dielectric functions and optical parameters of Si, Ge, GaP, GaAs, GaSb, InP, InAs, and InSb from 1.5 to 6.0 eV. *Phys. Rev. B* **1983**, *27*, 985–1009. [CrossRef]
46. Johnson, P.B.; Christy, R.W. Optical Constants of the Noble Metals. *Phys. Rev. B* **1972**, *6*, 4370–4379. [CrossRef]
47. Okazaki, T.; Sugimoto, H.; Hinamoto, T.; Fujii, M. Color Toning of Mie Resonant Silicon Nanoparticle Color Inks. *ACS Appl. Mater. Inter.* **2021**, *13*, 13613–13619. [CrossRef] [PubMed]
48. Mobley, C.D. *Light and Water: Radiative Transfer in Natural Waters*; Academic Press: Cambridge, MA, USA, 1994.
49. Nishi, H.; Tatsuma, T. Full-Color Scattering Based on Plasmon and Mie Resonances of Gold Nanoparticles Modulated by Fabry–Pérot Interference for Coloring and Image Projection. *ACS Appl. Nano Mater.* **2019**, *2*, 5071–5078. [CrossRef]
50. Wrigglesworth, E.G.; Johnston, J.H. Mie theory and the dichroic effect for spherical gold nanoparticles: An experimental approach. *Nanoscale Adv.* **2021**, *3*, 3530. [CrossRef]
51. Hogan, N.J.; Urban, A.S.; Ayala-Orozco, C.; Pimpinelli, A.; Nordlander, P.J.; Halas, N.J. Nanoparticles heat through light localization. *Nano Lett.* **2014**, *14*, 4640–4645. [CrossRef] [PubMed]
52. Loeb, S.K.; Li, C.; Kim, J.-H. Solar photothermal disinfection using broadband-light absorbing gold nanoparticles and carbon black. *Environ. Sci. Technol.* **2018**, *52*, 205–213. [CrossRef]